Ceramics International 51 (2025) 52409–52418

Contents lists available at ScienceDirect

Ceramics International

journal homepage: www.elsevier.com/locate/ceramint

# Nucleation and growth of $ZnAl_2O_4$ spinel phase in double-layered $Al_2O_3$/ZnO nanopillars and nanotubes prepared by atomic layer deposition

Gergő Vecsei [a,b], János J. Tomán [a,*], István Gábor Márián [a,d], Barbara Sárközi [a,b], Laura Juhász [a], Péter Pekker [c], Zoltán Erdélyi [a], Csaba Cserháti [a]

[a] Department of Solid State Physics, Faculty of Science and Technology, University of Debrecen, P.O. Box. 400, Debrecen, H-4002, Hungary
[b] Doctoral School of Physics, University of Debrecen, Debrecen, Hungary
[c] Nanolab, Research Institute of Biomolecular and Chemical Engineering, University of Pannonia, Egyetem st. 10, Veszprém, H-8200, Hungary
[d] Institute for Nuclear Research (ATOMKI), Bem tér 18/C, Debrecen, H-4026, Hungary

ARTICLE INFO

P. Vincenzini

*Keywords:*
Spinels
Nanowire
Computer simulations
Solid state reaction
Internal stress

ABSTRACT

Nucleation and growth kinetics of $ZnAl_2O_4$ spinel phase was studied between amorphous $Al_2O_3$ and crystalline ZnO oxide layers grown by atomic layer deposition on a highly curved solid Pt cores with Pt)$Al_2O_3$)ZnO) sequence (double-layered nanopillars, DLNPs). The composite pillars were annealed at 700 °C in ambient atmosphere for different durations. Thin plan-view lamellae were prepared from the cross sections of the pillars to investigate the nucleation and the growth kinetics of the $ZnAl_2O_4$ spinel phase in a transmission mode scanning electron microscope (TSEM). We found that similarly as in planar geometry, the growth occurs in two stages: first, islands form and grow along the interface until creating a continuous layer; then this continuous layer thickens. However, in comparison to the planar case, the first stage is extremely shortened due to the closed geometry. The growth rate of the formed continuous $ZnAl_2O_4$ phase is strongly influenced by the type of core (hollow in DLNTs, solid in DLNPs). The spinel layer grows parabolically with time, but much more slowly in DLNPs than in double-layered nanotubes (DLNTs). Computer simulations showed that the diffusion fluxes and the developing mechanical stresses in the system during the interdiffusion process explain the experimental findings.

## 1. Introduction

Although interdiffusion has been a known process for a long time and its technological importance is undeniable, it is still not fully understood. The details of the diffusion processes are becoming more and more important because of their increasing impact on material transport in nano-sized objects. In interdiffusion processes, material transport can lead to the development of internal stresses. The role of these stresses and their relaxation is more relevant as the sizes are reduced.

During interdiffusion, imbalanced atomic fluxes and the different partial molar volumes of the diffusing species, resulting in net volume flux, can lead to a build-up of internal stresses. As a result, an inhomogeneous deformation occurs, with one side of the diffusion couple contracting while the other expands. The possible formation of new phase(s) that induce a change in the specific volume in the reaction zone can also lead to stress development. The impact of these diffusion-induced stresses is highly influenced by the available relaxation mechanisms (e.g. Kirkendall shift, creep, dislocation slip, mechanical deformation) and their respective time scales with the diffusion annealing time. The developing internal stresses influence the driving force of the diffusion fluxes through the impact on the diffusion coefficient and on the thermodynamic potential of the diffusing species, i.e. the relaxation of this diffusion-induced stress leads to a feedback loop. All of these become increasingly important on the nanoscale.

One of the first attempts to address this problem was made by Larché and Cahn [1,2]. However, Stephenson [3] gave the first comprehensive set of differential equations that incorporate the minimum necessary fundamental phenomena. His model was formulated for planar geometry, included equations for calculating diffusion fluxes and the resulting compositional changes, as well as stress development caused by imbalanced atomic fluxes and different partial volumes, along with stress relaxation through plastic deformation.

Due to the long-range nature of the elastic fields, the geometry of the sample highly influences the process. Reactive diffusion on the nano-scale has gained significant importance in spherical geometry. Numerous studies have been published on the formation of hollow

* Corresponding author.
*E-mail address:* janos.toman@science.unideb.hu (J.J. Tomán).

https://doi.org/10.1016/j.ceramint.2025.08.446
Received 11 June 2025; Received in revised form 1 August 2025; Accepted 31 August 2025
Available online 8 September 2025

nano-shells (e.g. [4–6]), but the influence of stresses on these reactions was not studied, despite the significant role these processes might play in closed geometries with high curvatures.

The effect of closed geometry on the growth of intermetallic compound layers has been the subject of interest for some decades. One of the first experimental demonstrations, showing the importance of the effect, was performed in binary, cylindrical, Cd-Ni and Al-Cu diffusion couples of macroscopic dimensions (wires with a diameter of max. ~1 mm) [7–9]. The formation of the intermetallic phase, in the diffusion experiments, led to the appearance of cracks and local delamination of the intermetallic layers. Decreasing the diameter of the inner wire, a deviation was also observed from the parabolic behavior (that is, $\Delta x \propto k_p\sqrt{t}$, where $\Delta x$ is the thickness of the layer of the new phase, $k_p$ is the growth rate constant and $t$ is the annealing time). The difference in growth rate by changing the sequence of the layers was also described.

To illustrate the interplay between stress and solid state reactions, Schmitz et al. [10] designed a model experiment by performing thin-film diffusion in Al/Cu system building a tri-layered structure on atom probe tips with a 25 nm apex radius. Atom probe tomography (APT) analysis revealed that the growth of the reaction product varied consistently depending on the layer sequence. Theoretical descriptions of the observed phenomena have been published later by Erdélyi et al. [11] for spherical and by Roussel et al. [12] for cylindrical geometry.

As is known, during the reaction between amorphous $Al_2O_3$ and crystalline ZnO, the main diffusing species is ZnO [13,14]. As a result, diffusion is highly asymmetric and the $ZnAl_2O_4$ product phase grows at the expense of the amorphous alumina phase. In our earlier publications, we studied the kinetics of the $ZnAl_2O_4$ spinel growth in planar [15] and cylindrical [16] geometries.

In planar geometry, we demonstrated that the solid state reaction occurs in two stages. (i) first, islands of the new phase form with a thickness of ≈ 10 nm that grow laterally without significantly increasing their thickness; (ii) once these islands have grown together, they form a continuous layer that will thicken further.

In the cylindrical case, the effect of different stacking orders of ZnO and $Al_2O_3$ oxides deposited by atomic layer deposition (ALD) was studied in double-layered nanotubes (DLNTs). We showed that the phase grows parabolically over time, regardless of the layer sequence, however, the growth rate was higher in the )ZnO)$Al_2O_3$) stacking than in the reverse case. This difference was attributed to the competing vacancy fluxes induced by mechanical stress caused by the different specific volumes of the phases involved in the process, as well as the difference in diffusion fluxes of the two constituents.

In this paper, we present an experimental study of reactive diffusion between ALD-grown crystalline ZnO and amorphous $Al_2O_3$ oxide layers deposited on highly curved solid Pt pillars as cores with Pt)$Al_2O_3$)ZnO) sequence (double-layered nanopillars, DLNPs). In this geometry, one can expect the results to be curvature or radius dependent [11,12], therefore, we performed tests with different nominal core diameters. We show that phase growth occurs in two stages, but the first stage is extremely shortened and that the growth rate of the continuous spinel phase ($ZnAl_2O_4$) in the second stage is strongly influenced by the type of the core (hollow in DLNTs, solid in DLNPs).

After the interpretation of the experimental results, a hypothesis is formed that the developing stress is influenced by the type of core, which affects the growth rate of the spinel phase. We confirm our hypothesis via computer simulations using a theoretical framework developed on the basis of previously published models [11,12]. The theoretical details of the model are described in the following section.

## 2. Theoretical framework

### 2.1. Reactive diffusion in nanotubes and nanopillars

In [12], a model is described for reactive diffusion and stresses in nanowires or nanorods. In the present work, a modified version of this model for hollow and solid core double-layered systems is used to interpret the experimental results using computer simulations with parameters, initial and boundary conditions specific to the experiments. Fig. 1 displays the schematics of the DLNTs. Due to the geometry, the equations of the model are written in a cylindrical coordinate system using the radial distance ($r$), the azimuthal angle ($\theta$) and the signed distance along the main axis ($z$).

The formation of a new phase with a distinct specific volume compared to the parent phases during reactive diffusion causes significant strain. This yields the displacement vector for the cylinder with radius $r$ described by

$$u = \frac{1+\nu}{1-\nu}\frac{1}{r}I(r) + C_1 r + \frac{C_2}{r} - \nu\frac{C_3}{E}r, \tag{1}$$

where $\nu$ is Poisson's ratio, $E$ is Young's modulus, and

$$I(r) = \int_{R_i}^{r} \mathrm{r}\left[\varepsilon^{SF} + \frac{1-2\nu}{1+\nu}\left(\varepsilon^{P}_{rr} + A(\mathrm{r})\right)\right]\mathrm{dr}, \tag{2}$$

$$A(r) = 2\int_{R_i}^{r}\frac{\varepsilon^{P}_{rr}}{\mathrm{r}}\mathrm{dr}, \tag{3}$$

with $\varepsilon^{SF}$ denoting the stress-free expansion and $\varepsilon^{P}$ the plastic deformation. $C_1$, $C_2$ and $C_3$ represent the integration constants (determined from the boundary conditions) and $R_i$ denotes a lower limit for the integral, such as the inner radius of a hollow cylinder or the end of the solid core. The components of the strain and the stress tensors can then be determined:

$$\begin{aligned}
\sigma_{rr} &= -\frac{E}{1-\nu}\frac{1}{r^2}I(r) + \frac{E}{1+\nu}\left(A(r) + \frac{C_1}{1-2\nu} - \frac{C_2}{r^2}\right)\\
\sigma_{\theta\theta} &= \frac{E}{1-\nu}\frac{1}{r^2}I(r) - \frac{E}{1-\nu}\varepsilon^{SF} + \frac{E}{1+\nu}\left(\frac{\varepsilon^{P}_{rr}}{1-\nu} + \frac{\nu}{1-\nu}A(r) + \frac{C_1}{1-2\nu} + \frac{C_2}{r^2}\right)\\
\sigma_{zz} &= -\frac{E}{1-\nu}\varepsilon^{SF} + \frac{\nu E}{1+\nu}\left(\frac{\varepsilon^{P}_{rr} + A(r)}{1-\nu} + \frac{2}{1-2\nu}C_1\right) + \frac{1-\nu}{(1+\nu)(1-2\nu)}C_3.
\end{aligned} \tag{4}$$

The constants of integration ($C_1$, $C_2$, $C_3$) are obtained from the corresponding boundary conditions. For a system with a solid core and a free outer surface ($\sigma_{rr}(R_o) = 0$), the displacement at the interface with the core is equal to zero: $u(R_i) = 0$. If the wire is initially axially stressed with $\sigma^0_{zz}$, or when it is fixed only in the axial direction, then

$$\begin{aligned}
C_1 &= \frac{(1+\nu)(1-2\nu)}{1-\nu}\frac{1}{R_o^2}I(R_o) - (1-2\nu)A(R_o)\\
C_2 &= 0\\
C_3 &= \sigma^0_{zz}
\end{aligned} \tag{5}$$

as reported in [12]. However, if the cylinder is hollow (not discussed in [12]) and the inner surface is free too, then instead of $u(R_i) = 0$, the boundary condition becomes $\sigma_{rr}(R_i) = 0$. This yields the following constants of integration

$$\begin{aligned}
C_1 &= \frac{(1+\nu)(1-2\nu)}{1-\nu}\frac{1}{R_o^2 - R_i^2}I(R_o) - (1-2\nu)\frac{R_o^2}{R_o^2 - R_i^2}A(R_o)\\
C_2 &= \frac{C_1}{1-2\nu}R_i^2\\
C_3 &= \sigma^0_{zz}
\end{aligned} \tag{6}$$

However, when even the axial ends are free, then

$$\sigma_{zz} = -\frac{E}{1-\nu}\varepsilon^{SF} + \frac{\nu E}{1+\nu}\left(\frac{\varepsilon^{P}_{rr} + A}{1-\nu} + \frac{2}{1-2\nu}C_1\right), \tag{7}$$

so that $u_z = 0$ and for the last constant of integration ($C_3$) Eq. (A.3) from [12] must be used to have zero resultant force at the ends,

$$C_3 = \frac{2E}{1-\nu}\frac{1}{R_o^2}\int_{R_i}^{R_o}\mathrm{r}\,\varepsilon^{SF}\mathrm{dr} - \frac{2\nu E}{1+\nu}\left[\frac{1}{(1-\nu)R_o^2}\int_{R_i}^{R_o}\mathrm{r}\left(\varepsilon^{P}_{rr} + A(\mathrm{r})\right)\mathrm{dr} + \frac{1}{1-2\nu}C_1\right]. \tag{8}$$

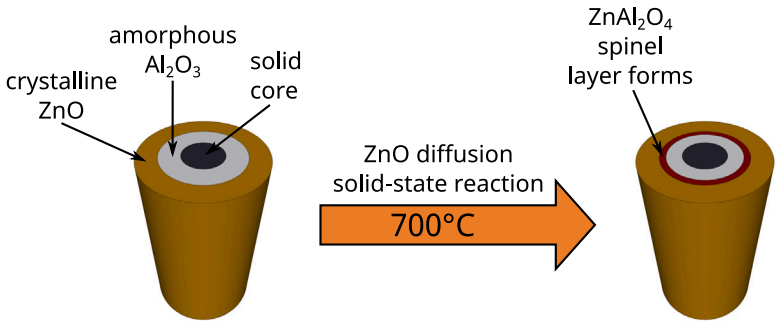


**Fig. 1.** Schematic representation of the double-layered nanopillars before and after heat treatment.

We show that the hollow or solid core of the cylinder can result in significant differences in the reaction-diffusion process.

To have a complete set of equations for the simulations, the stress-free volume change must be calculated as well using the formula

$$\frac{\mathrm{D}\varepsilon^{SF}}{\mathrm{D}t} = -\frac{1}{3}\left\{\frac{1}{r'}\sum_{i=1}^{n}\frac{\partial}{\partial r'}\left[r'(\Omega_i - \Omega_v)j_i\right] - q\right\}, \tag{9}$$

where $\mathrm{D}/\mathrm{D}t$ is the substantial derivative that provides the rate of change of any scalar quantity observed at a point that moves with the material coordinate system ($r'$). $\Omega_i$ is the atomic volume of component $i$ and $\Omega_v = \omega_v \sum_{i=1}^{n}(c_i\Omega_i)/\sum_{i=1}^{n} c_i$ is the atomic volume of a vacancy, $q$ is the change in volume, while the fluxes are

$$\vec{j}_i = -\rho\frac{\mathcal{D}_i}{kT}c_i c_v \nabla'\left[\left(\mu_i^{SF} + \Omega_i P\right) - \left(\mu_v^{SF} + \Omega_v P\right)\right] \quad \text{for } i = 1, \ldots, n, \tag{10}$$

in which the pressure is $P = -\frac{1}{3}\,\mathrm{tr}\,\hat{\sigma}$. $\mu_i$ and $\mu_v$ denote the chemical potentials of component $i$ and of the vacancy which can be determined from the Gibbs free enthalpy of the system, $\rho = 1/(\sum_{i=1}^{n} c_i\Omega_i + c_v\Omega_v)$ is the total atomic density, $\mathcal{D}_i = D_i^*/c_v^0$, with $D_i^*$ representing the tracer diffusion coefficient of the chemical component $i$ [11,17]; $k$ is Boltzmann's constant, $T$ is the absolute temperature, while $c_i$ and $c_v$ are the atomic fractions of component $i$ and the vacancies, with $c_v^0$ being the atomic fraction of the vacancies at equilibrium.

The composition over time, if fluxes flow only radially, changes according to

$$\frac{\mathrm{D}c_i}{\mathrm{D}t} = -\frac{1}{\rho r'}\frac{\partial}{\partial r'}\left(r' j_i\right) - c_i s_v, \tag{11}$$

where $s_v$ is the rate of change in the vacancy concentration caused by their creation/annihilation at the sinks and sources. Thus, the change in volume ($q$) has two contributions ($q = q_v + q_{sv}$), one due to the creation/annihilation of vacancies ($q_v$) and the other due to the change in specific volume caused by phase transformation ($q_{sv}$). The concentration and the rate of change of vacancies

$$c_v(P) = c_v^0 \exp\left(-\frac{\Omega_v P}{RT}\right), \tag{12}$$

$$s_v = K_r\left[c_v^0 \exp\left(-\frac{\Omega_v P}{RT}\right) - c_v\right], \tag{13}$$

where $K_r$ is a rate coefficient that describes the efficiency of the sources and sinks, $R$ is the gas constant. From these, $q_v$ can be obtained as $q_v = s_v\rho\Omega_v$.

The stress relaxation mechanisms are modeled together as plastic deformation, where only the radial component plays a role, which is given by

$$\dot{\varepsilon}_{rr}^{P} = \frac{1}{6\eta}(2\sigma_{rr} - \sigma_{\Theta\Theta} - \sigma_{zz}), \tag{14}$$

in which $\eta$ is the shear viscosity. For detailed derivation and explanation of the formulas in this section, see [12].

One has to solve these equations simultaneously for a double-layered )$Al_2O_3$)ZnO) cylindrical system using the appropriate parameters to observe the time evolution of stress, strain, displacement, vacancy concentration, fluxes, composition and hence the growth kinetics of a new $ZnAl_2O_4$ spinel phase in the material.

### 2.2. Implementation

To investigate whether the solid core and the developing stress can indeed significantly affect the growth rate of the spinel phase, computer simulations were performed using the theoretical model described above. The corresponding equations were solved numerically as described in [11,12].

Our objective was not to perfectly match the experimental data but to validate our hypothesis. We used the reduced (dimensionless) form of the equations. The input parameters are based on the available literature (see Table 1).

The nucleation phase was excluded from the modeling (it should be noted that the model elucidated in Section 2 would not be appropriate to address this phase). A continuous reaction layer was considered as the initial state and the developing stress profile and the formation time for this state was calculated using the equations described in Section 2. The thickness of the initial reaction layer was determined based on the experimental results and the theory available for the process.

The system is treated as a quasi-binary system, the two components being ZnO (Zn-ox) and $Al_2O_3$ (Al-ox). The $ZnAl_2O_4$ product phase is modeled as an ordered phase (with an existence range that is based on the experimentally determined composition profiles). The highly asymmetric diffusion is represented by ZnO diffusing 100 times faster than $Al_2O_3$ in the $ZnAl_2O_4$ phase. As a result, the product phase is growing mostly in one direction; at the expense of the alumina phase. Vacancy sinks and sources are located at the inner and outer surfaces of the bilayer (i.e. at $R_i$ and $R_o$), and also at the interfaces of the product phase.

We ran simulations with boundary conditions corresponding to both solid core geometry (see Eq. (5)) and hollow core geometry (see Eq. (6)), keeping every other parameter unchanged.

## 3. Experimental methods

Platinum nanopillars were built on silicon single-crystal wafers. The wafers were etched in 65 wt.% nitric acid for 5 min at room temperature to clean, then rinsed in distilled water for 5 min and 5 min in ethanol afterwards. The Pt nanopillars were fabricated using a gas injection system (GIS) in Thermo Fisher Scientific Scios 2 dual beam scanning electron microscope (FIB-SEM). The GIS precursor material was trimethyl(methylcyclopentadienyl)platinum(IV), which is decomposing when reacting with the electron beam. 5 kV acceleration voltage and 50 pA beam current was used for the electron-beam-induced deposition (EBID). The pillars were built in groups of four or six, in three different of diameters: 130 nm, 185 nm and 285 nm. This

**Table 1**
Parameters used in simulations to model the amorphous $Al_2O_3$ – crystalline ZnO system.

| Variable | Value | Description |
|---|---|---|
| $\nu$ | 0.24 | Poisson's ratio [18] |
| $E$ | 242 GPa | Young's modulus [19] |
| $R_i$ | 100 nm | Inner radius of the cylinder |
| $R_o$ | 300 nm | Outer radius of the cylinder |
| $n$ | 160 | Number of finite volume cells |
| $\sigma^0_{zz}$ | 0 | Initial stress in the axial direction |
| $\Omega_{Al_2O_3}$ | 35.2 $cm^3$/mol | Molar volume of $Al_2O_3$ [20] |
| $\Omega_{ZnO}$ | 15.5 $cm^3$/mol | Molar volume of ZnO [21] |
| $\omega_v$ | 75% | Relative volume of vacancies [22] |
| $q_{sv}$ | 4.5% | Relative change in specific volume caused by phase transformation [23] |
| $c^0_v$ | $10^{-5}$ | Atomic fraction of vacancies in equilibrium |
| $T$ | 973 K | Absolute temperature |
| $K_r$ | 1 | The efficiency of sources and sinks |
| $D_{ZnO}/D_{Al_2O_3}$ | 100 | Diffusion asymmetry in the $ZnAl_2O_4$ phase |
| $\eta_{Al_2O_3}$ | 0.15 $\frac{E\lambda^2}{D_{Al_2O_3}}$ | Stress relaxation of $Al_2O_3$ |
| $\eta_{ZnAl_2O_4}$ | 0.15 $\frac{E\lambda^2}{D_{Al_2O_3}}$ | Stress relaxation of $ZnAl_2O_4$ |
| $\eta_{ZnO}$ | 3.72 $\frac{E\lambda^2}{D_{Al_2O_3}}$ | Stress relaxation of ZnO |
| $dt$ | $4.5 \cdot 10^{-7} \frac{\lambda^2}{D_{Al_2O_3}}$ | Time step |

was followed by a degassing treatment in order to get rid of residual precursor gases in the Pt columns. The samples were heated at ~180 °C for 2 h in ambient atmosphere.

The fabricated Pt nanopillars were used as a cylindrical template. Thermal atomic layer deposition (ALD) technique was used to deposit 100–100 nm $Al_2O_3$ and ZnO layers on the Pt pillars in a Beneq TFS-200-186 reactor. ALD is a great tool to uniformly coat cylindrical templates, let them be nanowires or even nanotubes [16,24]. The $Al_2O_3$ layer was prepared at 100 °C using trimethylaluminium (TMA) and water ($H_2O$) as precursor materials. The pulse times for both TMA and $H_2O$ were 0.15 s, which were followed by 5 s nitrogen purges. For the ZnO layer, diethylzinc (DEZ) and water ($H_2O$) precursors were used at 125 °C. The pulse times were 0.15 s for both DEZ and water, followed by a 2.5 s and a 5 s nitrogen purge respectively. From our previous studies [15,16], we know that $Al_2O_3$ deposited this way is amorphous and ZnO has a hexagonal structure.

After deposition, the Pt)$Al_2O_3$)ZnO) structured cylindrical samples were heat treated in a tube furnace in ambient atmosphere. In order to compare the results with our earlier measurements on planar [15] and double-layered nanotube (DLNT) samples [16], we applied a two-stage thermal processing ('burn-out') [25]: (1) the temperature was increased from room temperature up to 230 °C with 10 °C/min heating rate, then (2) it was further increased up to 550 °C with a lowered (2 °C/min) heating rate. At 550 °C, the samples were removed from the furnace and cooled to room temperature. This pre-treatment was followed by the reaction–diffusion heat treatment at 700 °C in ambient atmosphere for various times: 0.5 h, 2 h, 4 h, 8 h, 12 h.

Plan-view TEM lamellae (parallel to the surface of the Si substrate, i.e. perpendicular to the longitudinal axis of the cylinders) were prepared from the composite nanopillars using the FIB-SEM equipment. Scanning transmission (TSEM) images were taken at 30 kV and 0.4/0.8 nA, with a retractable STEM detector. The detector operates in multiple modes, we employed the Bright Field (BF) and High-Angle Annular Dark-Field (HAADF) modes. In BF mode, the aperture is used to select the unscattered (transmitted) electrons, allowing for the structure being studied. While in HAADF mode, the electrons scattered at an angle of $> 5$ deg are collected and the image shows atomic number contrast (Z-contrast). The images were used to measure the thickness of the intermediate phase formed during the reaction–diffusion process. According to our previous studies [15,16], the product phase is $ZnAl_2O_4$ spinel. To confirm the existence of a spinel phase growing within these circumstances, we used a Talos F200X G2 scanning transmission electron microscope (STEM) equipped with a four-detector in-column energy dispersive X-ray (EDX) analysis system. We examined the samples with high-resolution scanning transmission electron microscopy (HRSTEM) and energy dispersive X-ray (EDX) spectrometry techniques as well.

## 4. Results

Fig. 2(a) shows the as-prepared composite nanopillars after the deposition of the oxide layers. It is visible that the hexagonal ZnO top layer has some surface roughness due to its polycrystalline nature. In Fig. 2(b), a cross-sectional image of a composite nanopillar is displayed after the deposition of the oxide layers. One can see, that $Al_2O_3$ has a smooth, cylindrical surface, while ZnO forms a nanograined shell around it. The grain structure shows a columnar nature, which is typical for ZnO layers grown by ALD [26].

We show cross-sectional TSEM images of composite nanopillars after heat treatment in Fig. 2(c-e), showing their inner structure. The images show a new phase between the initial $Al_2O_3$ and ZnO materials. From our previous studies [15,16], we learned from XRD measurements that this new phase is a $ZnAl_2O_4$ spinel phase. In Fig. 3, we show a HAADF STEM close-up of the reaction zone after 8 h of heat treatment at 700 °C with the corresponding EDX map of Al, O and Zn and a line scan across the diffusion zone. In Fig. 3 and the corresponding Table 2, we demonstrate the average compositions of the two parent phases and the product phase in the marked areas. These values correspond well to the expected compositions of $Al_2O_3$, $ZnAl_2O_4$ and ZnO, although both the composition profiles in Fig. 3 and the data in Table 2 show that the ZnO phase is not perfectly stoichiometric, but is oxygen-deficient. This is often the case with ZnO deposited by ALD [27].

In addition to its composition, the structure of the product phase was also investigated by HRSTEM measurements. Local Fast Fourier Transform (FFT) patterns from the diffusion zone show that the product phase is the ordered $ZnAl_2O_4$ intermediate phase with a spinel structure crystallized in the cubic $Fd\bar{3}m$ space group. Fig. 4(a) shows an HAADF STEM image taken along the $[0\,1\,1]_{fcc}$ direction of the reaction product. The FFT pattern demonstrates that the phase is the $ZnAl_2O_4$ spinel phase with $[0\,1\,1]_{fcc}$. The indexed lattice spacing of 4.1 Å and 2.9 Å are in agreement with the $(2\,0\,0)$ and $(0\,\bar{2}\,2)$ lattice planes of the spinel, respectively.

We performed 0.5 h long heat treatments to capture the earliest stage of phase formation. In some samples, we have seen continuous $ZnAl_2O_4$ layers (see Fig. 2(c)). We also found samples in which we could see discontinuous layers or islands of the product phase. In Fig.

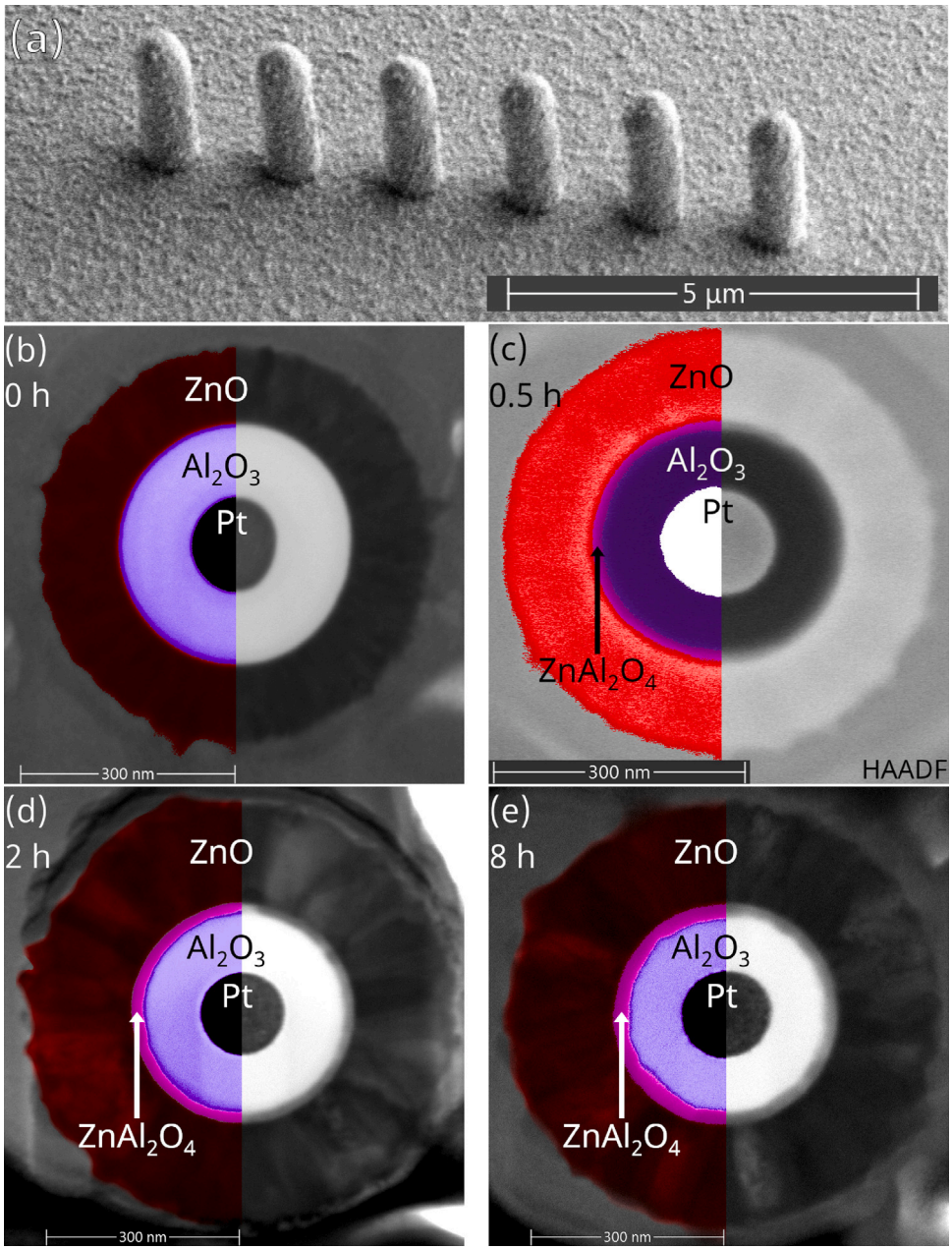


**Fig. 2.** Composite nanopillars (a) SEM image of a group of nanopillars. (b) Cross-section image of an as-deposited composite nano-pillar. On the solid, Pt core a smooth, 100 nm thick, amorphous $Al_2O_3$ shell is covered by a 100 nm thick, nanocrystalline ZnO layer. (c-e) Cross-sectional TSEM images of a nanopillars annealed at 700 °C for 0.5, 2, and 8 h. The reaction product is clearly visible between the two parent phases. For improved visibility, we used HAADF for the shortest annealing time. For easier interpretation, see the colored details in the image.

**Table 2**
The average compositions (in at.%) of the different regions marked in Fig. 3.

| | Area #1 $Al_2O_3$ | Area #2 $ZnAl_2O_4$ | Area #3 ZnO |
|---|---|---|---|
| O | 58.49 ± 4.79 at.% | 54.76 ± 3.52 at.% | 43.97 ± 3.25 at.% |
| Al | 41.43 ± 4.80 at.% | 31.09 ± 4.27 at.% | 0.70 ± 0.15 at.% |
| Zn | 0.08 ± 0.02 at.% | 14.14 ± 1.84 at.% | 55.33 ± 3.30 at.% |

5, we show the TEM image of one such example. Notice the highlighted and magnified image area which shows the spinel island.

For different heat treatment times, we measured the thicknesses of the $ZnAl_2O_4$ phases in the TSEM images, like the ones shown in Fig. 2(c-e). Detailed analysis of the product phase thicknesses could not reveal a definitive radius dependence in the investigated range. Probably, the uncertainties coming from other aspects of the experimental setup overwrite the curvature dependence. On the other hand, this is in agreement with previous findings, where the radius dependence was shown to be quite weak above 100 nm [11,12]. As a result, the data in

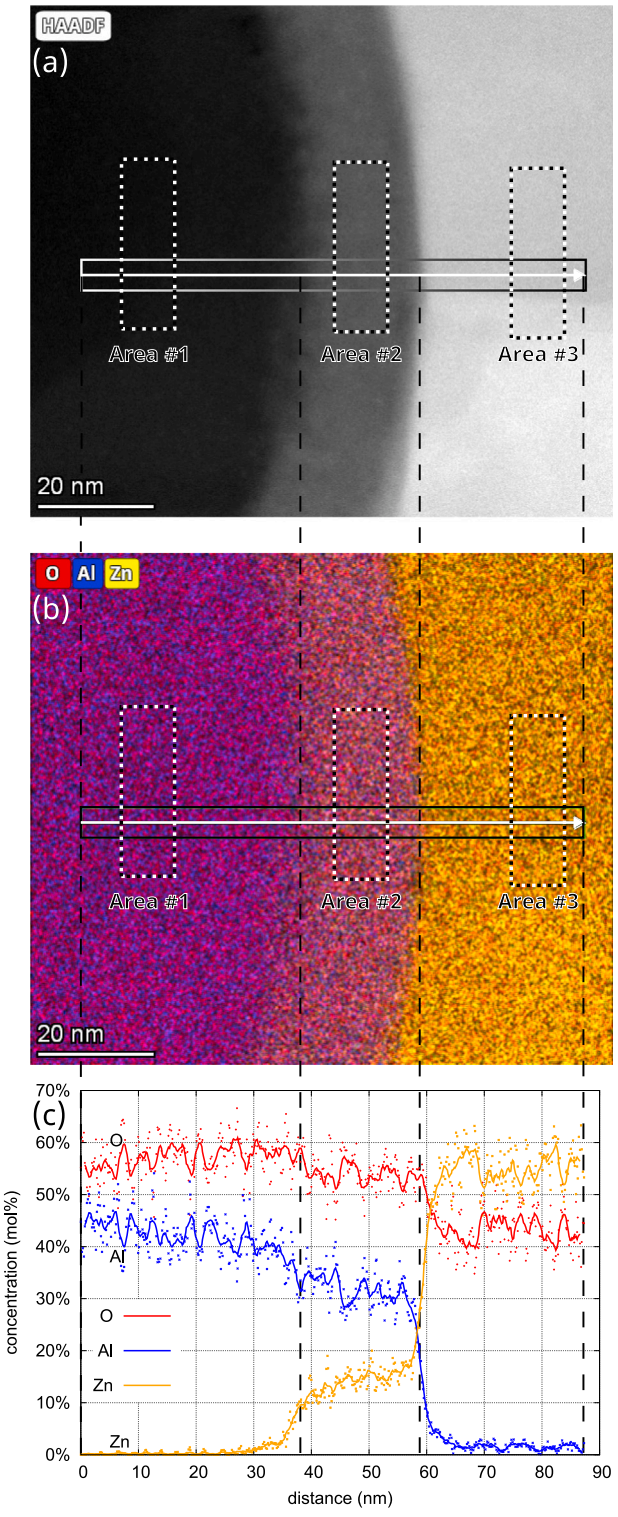


**Fig. 3.** EDX analysis of a sample after 8 h of heat treatment at 700°C. (a) HAADF TEM picture with the locations of the line profile and averaged area measurements for Table 2 marked. (b) Elemental EDX map with the same areas marked. (c) Elemental composition values from the area of the line profile (as dots) and the composition profiles calculated as moving averages using a 1.4 nm wide window (as continuous lines).

Fig. 6 represent the average phase thickness values over all core radii used for the experiments.

In Fig. 6, the measured layer thicknesses are plotted as a function of the square root of the corresponding annealing times. It can be seen that a straight line can be fitted to the measured values. The growth rate follows the parabolic law [28], that is, $\Delta x$ is a linear function of $\sqrt{t}$, where $\Delta x$ is the thickness of the layer of the new phase and $t$ is the annealing time. Because the formation of the continuous layer of the product phase is not always complete after 0.5 h, in Fig. 6, we did not include the value in the fitting of the growth rate, and in the graph we marked the average phase thickness at this time with an empty circle, although the data point still fits the growth rate trend well. The experimental data from our previous measurements performed in the same system, but without the solid core, i.e. in double-layered nanotubes (DLNTs) [16] are also plotted in the same graph (red squares). The plot shows that, although phase growth is parabolic in both cases, the formation of the new phase is faster in nanotubes with hollow cores and slower in nanopillars with solid cores.

## 5. Discussion

Studying the composition profiles in Fig. 3(c) and the quasi-binary composition profiles (indicating the fractions of the locally present atoms belonging to aluminium oxide and zinc oxide) in Fig. 7, we can gain some new insights into the phase formation process. We can see that ZnO can penetrate the amorphous $Al_2O_3$ almost 10 nanometers beyond the formed crystalline phase. According to the current theory of phase formation in a concentration gradient by the polymorphic nucleation mode [29], first, the two parent phases mix, creating a metastable solution; then, if the composition gradient decreases below a certain critical level, the new phase can form the new lattice structure by polymorphic transformation. Due to the gradient, pancake-shaped nuclei islands appear and they grow laterally until creating a continuous layer. The thickness of these pancake-shaped nuclei and the earliest continuous layer are around 10 nm [15,29]. This is the reason why, in the computer simulations, the thickness values start at 10 nm.

Furthermore, based on the quasi-binary composition profiles, we can determine the existence range of the spinel phase for the computer simulations. We set the existence range of the product phase between $c_{\text{Zn-ox}} = 0.214$ and $c_{\text{Zn-ox}} = 0.291$.

In planar samples, we observed the formation of $ZnAl_2O_4$ islands after 15 min. The average observed widths of the spinel islands were already in the 200 nm range after 15 min and in the 400 nm range after 30 min. Even after 1 h, we did not observe spinel phase as a continuous layer in planar samples. However, in DLNPs, after a 0.5 h long heat treatment, we observed a continuous $ZnAl_2O_4$ layer in several samples, which can be explained by the fact that the circumference of the $Al_2O_3$)ZnO interface is about 1000–1500 nm, so 2–4 spinel islands can already cover the cross-sectional image of the interface. Due to the statistical nature of both the phase formation process and the analysis, we also found samples in which we could see discontinuous layers or islands of the product phase. This proves that our findings about the two-stage phase formation process in planar samples are also valid in cylindrical geometry. However, due to the spatial constraint of the closed geometry, the length of the first stage is extremely reduced, and a continuous layer can form in a much shorter time than in planar samples.

In reaction–diffusion, a significant amount of stress can develop in the system. The two main contributing factors are: (i) the highly asymmetric nature of the diffusion, ZnO being the significantly faster diffuser; (ii) the increase in molar volume due to the formation of the new crystalline phase. However, in competition with developing stress, there are stress relaxation mechanisms at work in the system, too. ALD-deposited, amorphous $Al_2O_3$ is known to show a surprising level of plasticity [30], which can provide a very strong relaxation mechanism on the inner surface of the cylindrical system, if it is able to move, as in the case of hollow-core DLNTs. However, in the case of DLNPs, this relaxation mechanism is severely hindered.

Measurement of stress in samples is challenging, but highly asymmetric diffusion provides us with a very good stress indicator. The

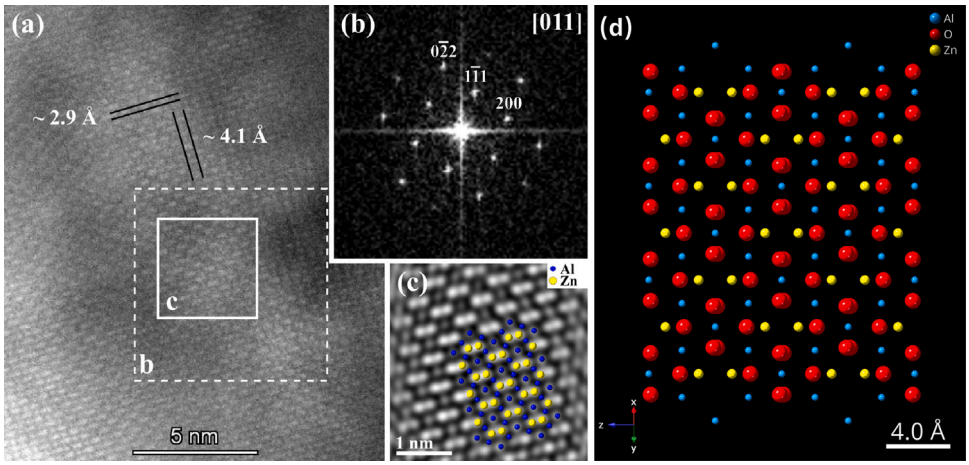


**Fig. 4.** High-resolution HAADF STEM image of the spinel structure of $ZnAl_2O_4$ phase. (a) High resolution HAADF STEM image of a reaction layer in the specimen annealed at 700°C for 8 h. (b) FFT pattern of the image area marked with the dashed rectangle, it shows [011] orientation of the $ZnAl_2O_4$ phase. (c) Lattice filtered inverse FFT image of the area marked with continuous rectangle, overlaid with the Zn-Al atomic arrangement of the $ZnAl_2O_4$ structural model in [011] orientation. (Lattice filtering was performed in DigitalMicrograph®.) (d) Structural model of $ZnAl_2O_4$ spinel in $[0\,1\,1]_{fcc}$ orientation.

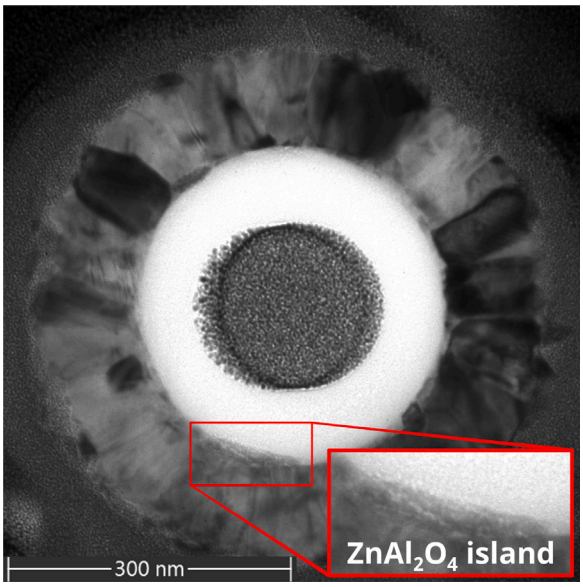


**Fig. 5.** TEM image of a DLNP annealed at 700 °C for 0.5 h. The magnified region shows a crystalline $ZnAl_2O_4$ spinel island.

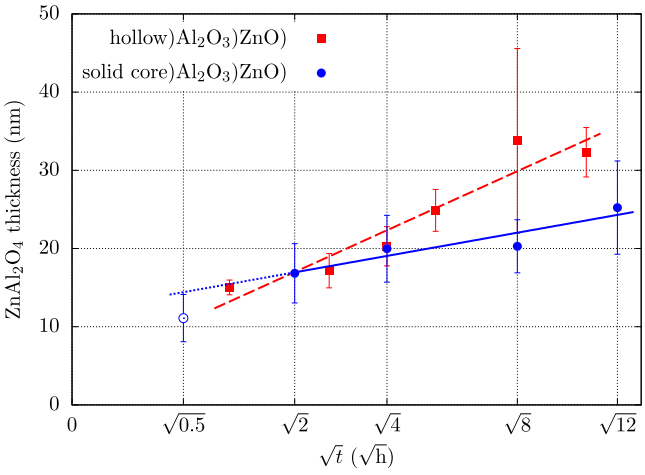


**Fig. 6.** Thickness of the $ZnAl_2O_4$ phase as a function of the square root of annealing time at 700 °C. The line of the solid core system (DLNPs) is fitted on the heat treatment values 2 h ≤ $t$ ≤ 12 h (solid blue points). Error bars show the ±2 standard deviation range. Source of the data for the hollow system (DLNTs) is [16].

crystalline ZnO – amorphous $Al_2O_3$ system is famous for the extremely strong Kirkendall-voiding that gives the system some of its application potential [13,14,31], creating hollow nanostructures through reaction–diffusion. According to the accepted theory of diffusion [28,32–34], pores can form in the reaction zone as a result of the vacancy flow oriented against the faster diffusing component. As ZnO is the faster diffusing component in this system, due of the Frenkel effect, voids (Kirkendall-voids) should appear on the ZnO side of the reaction product [35,36]. In both planar and hollow core cylindrical systems, we observed the formation of voids at the $ZnAl_2O_4$)ZnO interface from the very early stages of the reaction, as early as after 15 min of heat treatment. An analysis of our collected experimental data reveals no evidence of void presence within the cylindrical system with solid core. This implies that substantial compressive stress is likely developing, given the established understanding that high compressive stress can inhibit the formation of voids [37–39].

In Fig. 8, we show two snapshots from computer simulation results of the hollow core (DLNT) and solid core (DLNP) systems after the same amount of annealing time. It is clear that in the system with the solid core (Fig. 8(b)), the thickness of the product phase is significantly thinner than in the hollow system (Fig. 8(a)). This is in good agreement with the experimental findings. To gain some insight about the reason, we can look at the vacancy concentrations in the systems (see blue dashed lines in Fig. 8.) Due to the highly asymmetric diffusion and the developing stress field, a vacancy gradient develops which works against the interdiffusion, that is, the directions of the vacancy and ZnO concentration gradients are the same. In the case of the hollow core system, the developing difference in the vacancy concentration between the parent phases is much smaller than in the case of the solid core system. In cylindrical systems, there are two vacancy flux contributions that work against each other. One is induced by interdiffusion, pointing to the outer surface of the cylindrical sample, and the other emerges due to the stress field which develops during the process. The result of these two contributions significantly lowers the flux of ZnO in DLNPs

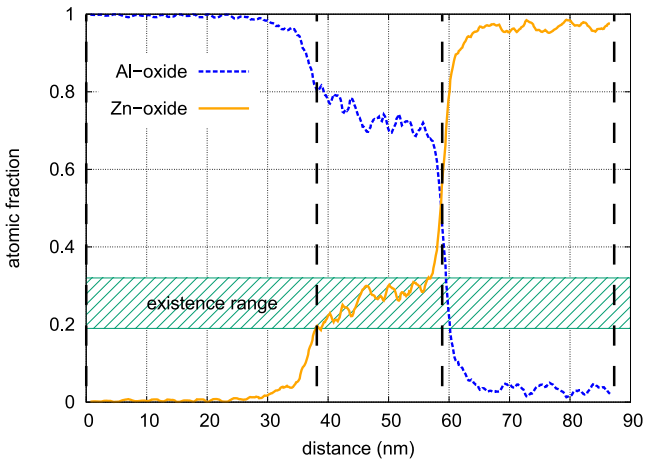


**Fig. 7.** The atomic composition profiles in Fig. 3 transformed into an effective binary system's composition profile. The vertical axis indicates what fraction of the locally present atoms belong to aluminium oxide and zinc oxide. The dashed lines mark the same interfaces as in Fig. 3(c). The existence range used in the computer simulations was determined on the basis of the hatched range of the composition profile.

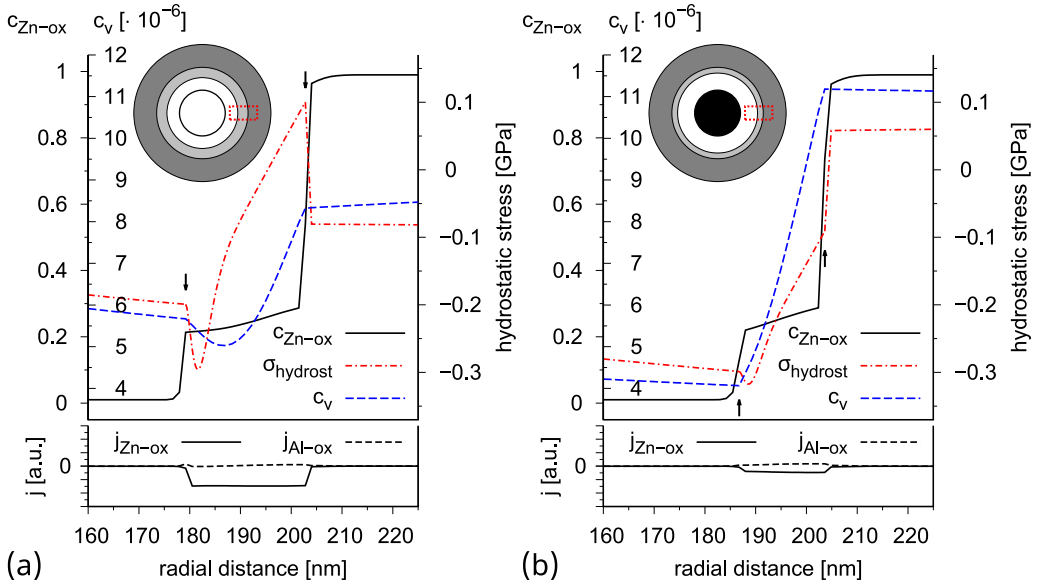


**Fig. 8.** Snapshots of computer simulations showing the composition profile of ZnO (continuous black line), vacancy composition (dashed blue line) and hydrostatic stress (dot-dashed red line) at the same moment for (a) hollow system and (b) solid core system. Arrows indicate the locations of the vacancy sinks and sources. The inserts are just schematic figures to represent the contents of the graphs.

compared to the DLNTs, because in that case the vacancy concentration gradient forming due to the stress field is significantly larger (see Fig. 8). Please note that at the $ZnAl_2O_4$)ZnO interface, the hydrostatic stress is in the tensile (positive) region for the hollow core system and in the compressive (negative) region for the solid core system. This explains our experimental findings as the formation of Kirkendall-voids is helped by the tensile stress in the hollow system, whereas it is suppressed by the compressive stress in the solid core system.

Fig. 9 shows the thickness of the spinel phase obtained from the computer simulations as a function of the square root of the annealing time. It can be seen that in both cases the growth follows the parabolic law. Furthermore, the growth rate is lower for DLNPs compared to DLNTs. These results align well with our experimental observations.

## 6. Conclusion

Samples with cylindrical geometry were prepared by atomic layer deposition on Pt nanopillars. The inner layer was amorphous $Al_2O_3$, the outer layer was crystalline ZnO. During heat treatment at 700°C, $ZnAl_2O_4$ spinel phase formed in a solid state reaction between the two parent phases.

We showed that phase growth occurs in two stages (i) first, islands of the new phase form with a thickness of ≈ 10 nm that grow along the interface without significantly increasing their thickness; (ii) once these islands have grown together, they form a continuous layer that will thicken further. The first stage of the reaction is extremely shortened due to the spatial constraints caused by the curved geometry.

Detailed analysis of the product phase thicknesses could not reveal a definitive radius dependence in the investigated range. We compared the growth rate with data from our previous work, in which the same system was studied in nanotubes with hollow core. We demonstrated that while the growth kinetics is parabolic in both cases, the presence or absence of a solid core significantly affects the growth rate of the $ZnAl_2O_4$ spinel product phase. Although Kirkendall-voids formed both in planar geometry and in double-layered nanotubes, we did not observe void formation in double-layered nanopillars with a solid core.

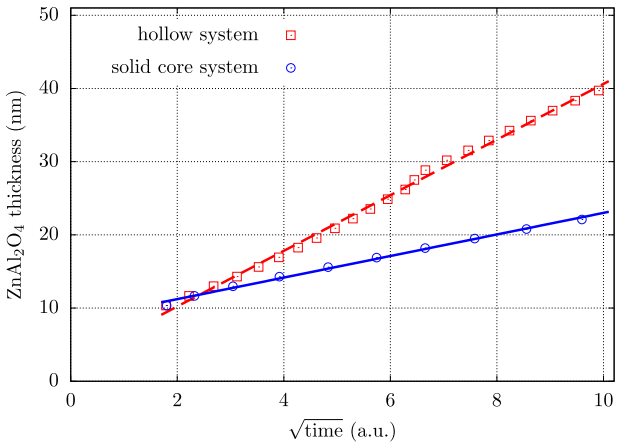


**Fig. 9.** The thickness of the product phase in computer simulations as a function of the square root of time. Red squares show the system with hollow center. Blue circles show the case with a solid core in the middle. The corresponding lines are linear fits of the points.

This is a strong indication of the presence of compressive stress in the system. We performed computer simulations based on the available continuum theory, introducing different boundary conditions for hollow and solid core systems. The simulation results confirmed the accumulation of a significant amount of compressive stress and a slower growth rate of the product phase when the system has a solid core.

## CRediT authorship contribution statement

**Gergő Vecsei:** Writing – review & editing, Writing – original draft, Visualization, Methodology, Investigation, Formal analysis, Data curation. **János J. Tomán:** Writing – review & editing, Writing – original draft, Visualization, Validation, Software, Methodology, Investigation, Formal analysis, Data curation, Conceptualization. **István Gábor Márián:** Writing – review & editing, Writing – original draft, Visualization, Validation, Software, Methodology, Investigation, Formal analysis, Data curation. **Barbara Sárközi:** Investigation, Formal analysis, Data curation. **Laura Juhász:** Visualization, Investigation. **Péter Pekker:** Visualization, Methodology, Investigation, Formal analysis, Data curation. **Zoltán Erdélyi:** Writing – review & editing, Writing – original draft, Visualization, Supervision, Software, Resources, Conceptualization. **Csaba Cserháti:** Writing – review & editing, Writing – original draft, Visualization, Validation, Supervision, Resources, Project administration, Funding acquisition, Formal analysis, Data curation, Conceptualization.

## Declaration of competing interest

The authors declare that they have no known competing financial interests or personal relationships that could have appeared to influence the work reported in this paper.

## Acknowledgments

This work was supported by the Development and Innovation Office NKFIH, Grant No.: OTKA.K143724. Supported by the University of Debrecen Program for Scientific Publication. TEM measurements were performed at the Nanolab, Research Institute of Biomolecular and Chemical Engineering, University of Pannonia.

## References

[1] F. Larcht'e, J. Cahn, The effect of self-stress on diffusion in solids, Acta Metall. 30 (10) (1982) 1835–1845, http://dx.doi.org/10.1016/0001-6160(82)90023-2, URL https://www.sciencedirect.com/science/article/pii/0001616082900232.

[2] F. Larché, J. Cahn, Overview no. 41 the interactions of composition and stress in crystalline solids, Acta Metall. 33 (3) (1985) 331–357, http://dx.doi.org/10.1016/0001-6160(85)90077-X, URL https://www.sciencedirect.com/science/article/pii/000161608590077X.

[3] G. Stephenson, Deformation during interdiffusion, Acta Metall. 36 (10) (1988) 2663–2683.

[4] Y. Yin, R.M. Rioux, C.K. Erdonmez, S. Hughes, G.A. Somorjai, A.P. Alivisatos, Formation of hollow nanocrystals through the nanoscale kirkendall effect, Science 304 (5671) (2004) 711–714, http://dx.doi.org/10.1126/science.1096566, arXiv:https://www.science.org/doi/pdf/10.1126/science.1096566.

[5] G. Glodán, C. Cserháti, I. Beszeda, D.o.L. Beke, Production of hollow hemisphere shells by pure kirkendall porosity formation in Au/Ag system, Appl. Phys. Lett. 97 (11) (2010) 113109, http://dx.doi.org/10.1063/1.3490675, arXiv:https://pubs.aip.org/aip/apl/article-pdf/doi/10.1063/1.3490675/13157131/113109_1_online.pdf.

[6] G. Glodán, C. Cserháti, D. o L. Beke, Temperature-dependent formation and shrinkage of hollow shells in hemispherical Ag/Pd nanoparticles, Phil. Mag. 92 (31) (2012) 3806–3812, http://dx.doi.org/10.1080/14786435.2012.687841.

[7] Y. Geguzin, Aspects of cavity formation during interdiffusion in specimens of'closed' shape, Fiz. Met. Metalloved. 43 (3) (1977) 602–609.

[8] L. Kozéky, D.L. Beke, Suppressed layer growth of intermetallic phases in cylindrical cd-Ni diffusion couples, in: Diffusion in Materials - DIMAT 1992, in: Defect and Diffusion Forum, 95, Trans Tech Publications Ltd, 1993, pp. 605–610, http://dx.doi.org/10.4028/www.scientific.net/DDF.95-98.605.

[9] D.L. Beke, L. Kozéky, I. Gődény, F. Kedves, Effect of stress and macroscopic deformation caused by interdiffusion on the growth of intermetallic layers, in: Diffusion in Metals and Alloys (DIMETA 88), in: Defect and Diffusion Forum, 66, Trans Tech Publications Ltd, 1990, pp. 1357–1364, http://dx.doi.org/10.4028/www.scientific.net/DDF.66-69.1357.

[10] G. Schmitz, C.-B. Ene, C. Nowak, Reactive diffusion in nanostructures of spherical symmetry, Acta Mater. 57 (9) (2009) 2673–2683, http://dx.doi.org/10.1016/j.actamat.2009.02.021, URL https://www.sciencedirect.com/science/article/pii/S1359645409001037.

[11] Z. Erdélyi, G. Schmitz, Reactive diffusion and stresses in spherical geometry, Acta Mater. 60 (4) (2012) 1807–1817, http://dx.doi.org/10.1016/j.actamat.2011.12.006, URL https://www.sciencedirect.com/science/article/pii/S1359645411008688.

[12] M. Roussel, Z. Erdélyi, G. Schmitz, Reactive diffusion and stresses in nanowires or nanorods, Acta Mater. 131 (2017) 315–322, http://dx.doi.org/10.1016/j.actamat.2017.04.001, URL https://www.sciencedirect.com/science/article/pii/S1359645417302847.

[13] H. Jin fan, M. Knez, R. Scholz, K. Nielsch, E. Pippel, D. Hesse, M. Zacharias, U. Gösele, Monocrystalline spinel nanotube fabrication based on the kirkendall effect, Nat. Mater. 5 (8) (2006) 627–631, http://dx.doi.org/10.1038/nmat1673.

[14] H.J. Fan, M. Knez, R. Scholz, D. Hesse, K. Nielsch, M. Zacharias, U. Gösele, Influence of Surface Diffusion on the Formation of Hollow Nanostructures Induced by the Kirkendall Effect: The Basic Concept, Nano Lett. 7 (4) (2007) 993–997, http://dx.doi.org/10.1021/nl070026p.

[15] G. Jáger, J.J. Tomán, L. Juhász, G. Vecsei, Z. Erdélyi, C. Cserháti, Nucleation and growth kinetics of ZnAl2O4 spinel in crystalline ZnO – amorphous Al2O3 bilayers prepared by atomic layer deposition, Scr. Mater. 219 (2022) 114857, http://dx.doi.org/10.1016/j.scriptamat.2022.114857, URL https://www.sciencedirect.com/science/article/pii/S1359646222003530.

[16] G. Vecsei, G. Jáger, L. Juhász, J.J. Tomán, V.O. Odhiambo, I.M. Szilágyi, Z. Erdélyi, C. Cserháti, Effect of stacking order in cylindrical geometry on the growth of ZnAl2O4 spinel phase, Materialia 30 (2023) 101819, http://dx.doi.org/10.1016/j.mtla.2023.101819, URL https://www.sciencedirect.com/science/article/pii/S2589152923001461.

[17] H. Mehrer, The Effect of Pressure on Diffusion, Defect Diffus. Forum 129–130 (1996) 57–76, http://dx.doi.org/10.4028/www.scientific.net/DDF.129-130.57, URL https://www.scientific.net/DDF.129-130.57.

[18] J. Proost, F. Spaepen, Evolution of the growth stress, stiffness, and microstructure of alumina thin films during vapor deposition, J. Appl. Phys. 91 (1) (2002) 204–216, http://dx.doi.org/10.1063/1.1425076, arXiv:https://pubs.aip.org/aip/jap/article-pdf/91/1/204/19149766/204_1_online.pdf.

[19] N.J. van der Laag, M.D. Snel, P.C.M.M. Magusin, G. de With, Structural, elastic, thermophysical and dielectric properties of zinc aluminate (ZnAl2O4), J. Eur. Ceram. Soc. 24 (8) (2004) 2417–2424, http://dx.doi.org/10.1016/j.jeurceramsoc.2003.06.001, URL https://www.sciencedirect.com/science/article/pii/S0955221903006277.

[20] M.D. Groner, F.H. Fabreguette, J.W. Elam, S.M. George, Low-temperature al2o3 atomic layer deposition, Chem. Mater. 16 (4) (2004) 639–645, http://dx.doi.org/10.1021/cm0304546.

[21] J. Yang, A. Bahrami, X. Ding, S. Lehmann, N. Kruse, S. He, B. Wang, M. Hantusch, K. Nielsch, Characteristics of ALD-ZnO thin film transistor using H2O and H2O2 as oxygen sources, Adv. Mater. Interfaces 9 (15) (2022) 2101953, http://dx.doi.org/10.1002/admi.202101953, URL arXiv:https://advanced.onlinelibrary.wiley.com/doi/pdf/10.1002/admi.202101953.

[22] N. Gladkikh, A. Kryshtal, Evaluation of the Relative Volume of a Vacancy, Phys. Met. Met. 85 (1998).

[23] S. Mandal, J.G. Hemrick, M.K. Mahapatra, Zinc aluminate (ZnAl2O4) refractory aggregates: Dilatometric, sintering studies and thermal expansion coefficient, J. Eur. Ceram. Soc. 42 (13) (2022) 6244–6254, http://dx.doi.org/10.1016/j.jeurceramsoc.2022.06.058, URL https://www.sciencedirect.com/science/article/pii/S095522192200509X.

[24] Q. Peng, X.-Y. Sun, J.C. Spagnola, C. Saquing, S.A. Khan, R.J. Spontak, G.N. Parsons, Bi-directional Kirkendall Effect in Coaxial Microtube Nanolaminate Assemblies Fabricated by Atomic Layer Deposition, ACS Nano 3 (3) (2009) 546–554, http://dx.doi.org/10.1021/nn8006543.

[25] O. Kéri, E. Kocsis, Z.K. Nagy, B. Parditka, Z. Erdélyi, I.M. Szilágyi, Preparation of $Al_2O_3$ coated PVA and PVP nanofibers and $Al_2O_3$ nanotubes by electrospinning and atomic layer deposition, Rev. Roum. de Chim. 63 (2018) 401–406, URL http://revroum.lew.ro/wp-content/uploads/2018/05/Art05.pdf.

[26] A. Seweryn, R. Pietruszka, B.S. Witkowski, A. Wierzbicka, R. Jakiela, P. Sybilski, M. Godlewski, Structural and electrical parameters of ZnO thin films grown by ald with either water or ozone as oxygen precursors, Crystals 9 (11) (2019) http://dx.doi.org/10.3390/cryst9110554, URL https://www.mdpi.com/2073-4352/9/11/554.

[27] V. Gurylev, T.P. Perng, Defect engineering of ZnO: Review on oxygen and zinc vacancies, J. Eur. Ceram. Soc. 41 (10) (2021) 4977–4996, http://dx.doi.org/10.1016/j.jeurceramsoc.2021.03.031, URL https://www.sciencedirect.com/science/article/pii/S0955221921001801.

[28] J. Philibert, Atom Movements, Diffusion and Mass Transport in Solids, Les Editions de Physique, Les Ulis, France, 1991.

[29] A.M. Gusak, Y.A. Lyashenko, S.V. Kornienko, M.O. Pasichnyy, A.S. Shirinyan, T.V. Zaporozhets, Diffusion-Controlled Solid State Reactions, Wiley-VCH Verlag GmbH & Co. KGaA, 2010, http://dx.doi.org/10.1002/9783527631025.

[30] E.J. Frankberg, A. Lambai, J. Zhang, J. Kalikka, S. Khakalo, B. Paladino, M. Cabrioli, N.G. Mathews, T. Salminen, M. Hokka, J. Akola, A. Kuronen, E. Levänen, F. Di Fonzo, G. Mohanty, Exceptional microscale plasticity in amorphous aluminum oxide at room temperature, Adv. Mater. 35 (46) (2023) 2303142, http://dx.doi.org/10.1002/adma.202303142, URL arXiv:https://advanced.onlinelibrary.wiley.com/doi/pdf/10.1002/adma.202303142.

[31] E. Shkondin, H. Alimadadi, O. Takayama, F. Jensen, A.V. Lavrinenko, Fabrication of hollow coaxial Al2O3/ZnAl2O4 high aspect ratio freestanding nanotubes based on the Kirkendall effect, J. Vac. Sci. Technol. A: Vac. Surfaces, Films 38 (1) (2020) 13402, http://dx.doi.org/10.1116/1.5130176.

[32] Y. Yin, C.K. Erdonmez, A. Cabot, S. Hughes, A.P. Alivisatos, Colloidal Synthesis of Hollow Cobalt Sulfide Nanocrystals, Adv. Funct. Mater. 16 (11) (2006) 1389–1399, http://dx.doi.org/10.1002/adfm.200600256, URL https://onlinelibrary.wiley.com/doi/abs/10.1002/adfm.200600256.

[33] J. Svoboda, F.D. Fischer, Stress development during reaction of metallic nanospheres with gas, Acta Mater. 59 (1) (2011) 61–67, http://dx.doi.org/10.1016/j.actamat.2010.09.001, URL https://www.sciencedirect.com/science/article/pii/S1359645410005665.

[34] G.E. Murch, A.V. Evteev, E.V. Levchenko, I.V. Belova, Recent progress in the simulation of diffusion associated with hollow and bi-metallic nanoparticles, Diffus. Fundam. 11 (2009) 1–22, http://dx.doi.org/10.62721/diffusion-fundamentals.11.494.

[35] A.M. Gusak, N.V. Storozhuk, Competition of k and f sinks during void formation, Phys. Met. Met. 114 (3) (2013) 197–206, http://dx.doi.org/10.1134/S0031918X13030071.

[36] A.M. Gusak, A. Titova, New thermodynamic approaches to failure analysis in microelectronic materials, Cherkasy Univ. Bull.: Phys. Math. Sci. 1 (1) (2022) 33–46, http://dx.doi.org/10.31651/2076-5851-2022-33-46, URL https://phys-ejournal.cdu.edu.ua/article/view/4878.

[37] I. Szabó, D.L. Beke, Effect of stress on diffusion, in: Diffusion in Materials - DIMAT 1992, in: Defect and Diffusion Forum, vol. 95, Trans Tech Publications Ltd, 1993, pp. 537–554, http://dx.doi.org/10.4028/www.scientific.net/DDF.95-98.537.

[38] L. Daróczi, D. Beke, G. Langer, G. Radnóczi, Z. Czigány, Effect of low hydrostatic pressures on the solid state reactions in multilayers, J. Magn. Magn. Mater. 156 (1) (1996) 417–418, http://dx.doi.org/10.1016/0304-8853(95)00921-3, Proceedings of the Second International Symposium on Metallic Multilayers. URL https://www.sciencedirect.com/science/article/pii/0304885395009213.

[39] J. Wojewoda-Budka, I. Kwiecien, A. Bigos, S. Terlicka, L. Litynska-Dobrzynska, P. Petrzak, A. Wierzbicka-Miernik, M. Szczerba, Z. Szulc, E. Rabkin, How to suppress the Kirkendall porosity within the Ti/Ni explosive welds? Arch. Civ. Mech. Eng. 24 (2) (2024) 117, http://dx.doi.org/10.1007/s43452-024-00887-9, URL https://doi.org/10.1007/s43452-024-00887-9.